scientific reports

Check for updates

OPEN

A hydrated 2,3-diaminophenazinium chloride as a promising building block against SARS-CoV-2

Rajani Kanta Mahato[1], Ayan Kumar Mahanty[2], Muddukrishnaiah Kotakonda[3], Sunnapu Prasad[4], Subires Bhattacharyya[5]✉ & Bhaskar Biswas[1]✉

Phenazine scaffolds are the versatile secondary metabolites of bacterial origin. It functions in the biological control of plant pathogens and contributes to the producing strains ecological fitness and pathogenicity. In the light of the excellent therapeutic properties of phenazine, we have synthesized a hydrated 2,3-diaminophenazinium chloride ($DAPH^+Cl^-·3H_2O$) through direct catalytic oxidation of *o*-phenylenediamine with an iron(III) complex, $[Fe(1,10\text{-phenanthroline})_2Cl_2]NO_3$ in ethanol under aerobic condition. The crystal structure, molecular complexity and supramolecular aspects of $DAPH^+Cl^-$ were confirmed and elucidated with different spectroscopic methods and single crystal X-ray structural analysis. Crystal engineering study on $DAPH^+Cl^-$ exhibits a fascinating formation of $(H_2O)_2…Cl^-…(H_2O)$ cluster and energy framework analysis of defines the role of chloride ions in the stabilization of $DAPH^+Cl^-$. The bactericidal efficiency of the compound has been testified against few clinical bacteria like *Streptococcus pneumoniae*, *Escherichia coli*, *K. pneumoniae* using the disc diffusion method and the results of high inhibition zone suggest its excellent antibacterial properties. The phenazinium chloride exhibits a significant percentage of cell viability and a considerable inhibition property against SARS-CoV-2 at non-cytotoxic concentration compared to remdesivir. Molecular docking studies estimate a good binding propensity of $DAPH^+Cl^-$ with non-structural proteins (nsp2 and nsp7-nsp-8) and the main protease (M^{pro}) of SARS-CoV-2. The molecular dynamics simulation studies attribute the conformationally stable structures of the $DAPH^+Cl^-$ bound M^{pro} and nsp2, nsp7-nsp8 complexes as evident from the considerable binding energy values, − 19.2 ± 0.3, − 25.7 ± 0.1, and − 24.5 ± 0.7 kcal/mol, respectively.

The relentless outbreak of the novel coronavirus infection caused by severe acute respiratory syndrome coronavirus 2 (SARS-CoV-2) shatters human life and health to a severe extent throughout the world[1]. The infection caused by the novel coronaviruses is not only limited to humans and mammals, but birds are also a sufferer of this disease. Among the identified viral species, six coronavirus species are SARS-CoV, MERS-CoV, HCoV-229E, HCoV-NL63, HCoV-OC43 and HCoV-HKU1 induce severe damage to the living body[2,3]. It is documented that in late 2019, a viral respiratory illness was caused and rapidly spread by SARS-CoV-2 as named by the International Committee of Taxonomy of Viruses (ICTV)[4]. The 2019-nCoV virus is believed to belong to the genus beta-coronavirus of the family Coronaviridae. The 2019-nCoV adopts a single strand, positive-sense ribonucleic acid (RNA) genome and is thought to be originated from bats (Fig. 1)[5–7]. The clinical manifestations of COVID-19 suggest that the disease spreads through respiratory droplets of the infected individuals and leads to life-threatening conditions, including invasive lesions in the lungs leading to a serious threat to human civilizations and the living world[8–12]. On 12 March 2020, the World Health Organization (WHO) declared the COVID-19 a pandemic[13].

More surprisingly, the disease in the second pandemic wave displays more aggravation leading to acute respiratory failure, sepsis and death[14–17]. The multiple factors like an exacerbated inflammatory reaction, importunate

[1]Department of Chemistry, University of North Bengal, Darjeeling 734013, India. [2]Department of Biotechnology, University of North Bengal, Darjeeling 734013, India. [3]Department of Technology, Anna University, Chennai 600025, India. [4]Department of Pharmaceutical Chemistry, Sri Ramakrishna Institute of Paramedical Science, Coimbatore 641044, India. [5]Vice-Chancellor, University of North Bengal, Darjeeling 734013, India. ✉email: subires.bhattacharyya@gmail.com; bhaskarbiswas@nbu.ac.in

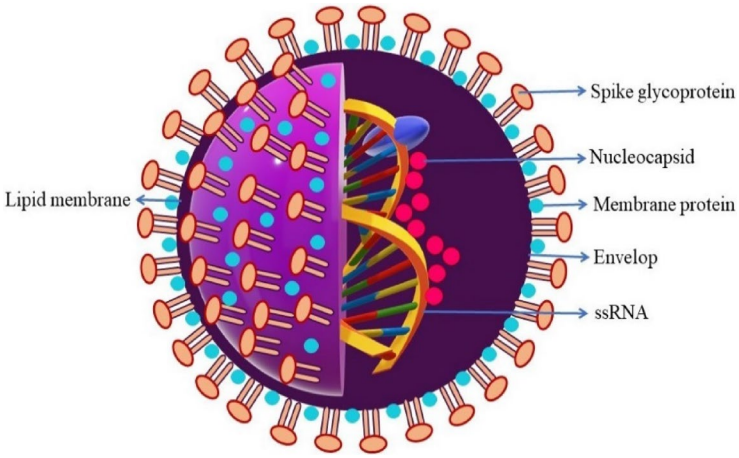

Figure 1. Schematic diagram of SARS-CoV-2.

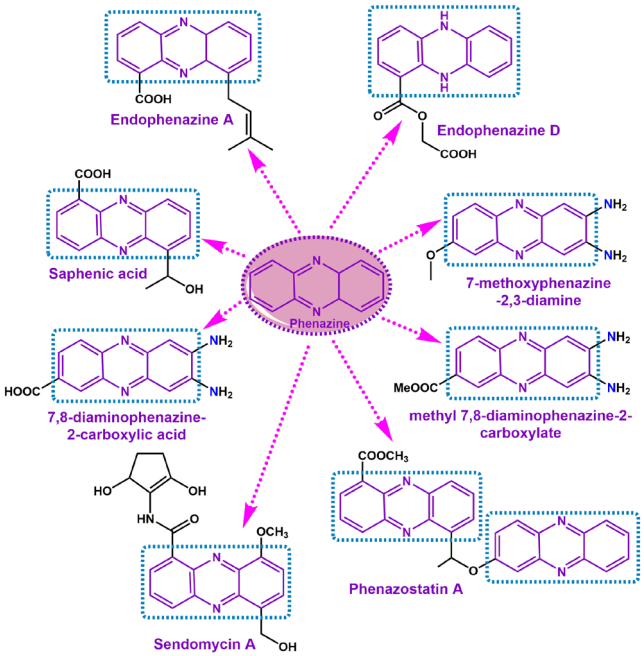

Figure 2. Representative examples of drugs comprising phenazine pharmacophore.

viral load and flawed antiviral defense pathways are responsible[14–18]. Therefore, exploring the underlying cellular mechanisms is of supreme significance to shed off the COVID-19 physiopathology and develop appropriate therapies. The considerable efforts made in scientific research during the last 2 years in developing therapeutic agents and treatment processes are genuinely praiseworthy[19–25]. However, the vast population, lack of awareness, and limited medicinal resources (medicines, vaccines, and medical staff) impose various restrictions to recover this pandemic. Therefore, valuable inputs from the scientific community may advance medical science to a greater extent.

Scientific literature suggests that phenazine is an important class of natural products found in nature. It has excellent medicinal importance. More than 6000 phenazine-based compounds are reported in the last century, and the number is increasing day by day for its clinical and therapeutical efficacy (Fig. 2). Several naturally found phenazines are isolated from gram-positive and gram-negative pathogens, from soil habitants and marine habitats[26,27]. Phenazines are commonly important for their antibiotic[28], antitumor[29], antiparasitic[30] and antimalarial[31] properties. Besides that, this redox-active nitrogen-containing heterocyclic pigment balances the redox activities inside their producers[32,33].

Under the gravity of rapid evolution and the uncontrollable expansion of SARS-CoV-2, we have synthesized a novel hydrated phenazinium chloride salt through a catalytic oxidative coupling of OPD in a pure single crystalline phase. The compound has been characterized with a suite of spectroscopic methods and single crystal X-ray

diffraction study. Further, the bio-potency of the compound has been evaluated through in vitro bactericidal and in vitro antiviral studies against few bacterial species and 1 × 10e4VeroE6 cells, respectively. Detailed molecular docking and MD simulation studies are also carried out in triplicate to reveal the binding propensities and stability of the hydrated phenazine chloride bound M^{pro}, nsp2 and nsp7-nsp8 complexes.

Methods and modeling

Preparation of the 2,3-diaminophenazinium chloride ($DAPH^+Cl^-$). *Chemicals, solvents and starting materials.* High purity o-phenylenediamine (TCI, Japan), ferric chloride (SRL, India), o-phenanthroline (Merck, India) and ammonium ceric(IV) nitrate and other reagents were purchased from respective outlets. All the used chemicals and reagents were of analytical grade.

Synthesis of hydrated $DAPH^+Cl^-$. A previously reported mononuclear iron(III) complex[34] was used as a catalyst to prepare 2,3-diaminophenazine (DAP) in high yield. o-phenylenediamine (1.08 g, 10 mmol) was added to iron(III) complex (0.55 g, mmol) in a 10:1 mol ratio in ethanol followed by passing of 300 air bubbles with a syringe, and after that, the mixture was kept for slow stirring for 10 h. The pale yellow crystallized product was extracted from the reaction mixture. The compound was recrystallized in an aqueous-ethanol medium. The suitable single crystals were dried in a vacuum over a silica gel indicator.

Isolated yield = 0.910 g (84.2%). Anal. Calc. for $C_{12}H_{17}N_4O_3Cl$ ($DAPH^+Cl^-$): C, 47.92; H, 5.70; N, 18.62; Found: C, 47.97; H, 5.76; N, 18.69. IR (KBr, cm^{-1}; Fig. S1): 3412 ($\nu_{O\text{-}H}$), 3149 ($\nu_{N\text{-}H}$), 1624($\nu_{C=N}$); UV–Vis (λ_{max}, nm; Fig. S2): 258, 426; ^{1}HNMR (DMSO-d_6): δ7.64–7.97 [6H, Ar–*H*], δ6.95 [4H,N*H*$_2$].

Physical measurements. FTIR-8400S SHIMADZU spectrometer (Shimadzu, Kyoto, Japan) was employed to record IR spectrum of the $DAPH^+Cl^-$ product ranging from 400 to 3600 cm^{-1}. ^{1}H and ^{13}C NMR spectra of the $DAPH^+Cl^-$ were obtained on a Bruker Advance 400 MHz spectrometer (Bruker, Massachusetts, USA) in $CDCl_3$at 298 K. Steady-state absorption and other spectral data were obtained on a JASCO V-730 UV–Vis spectrophotometer (Jasco, Tokyo, Japan). A Perkin Elmer 2400 CHN microanalyzer (Perkin Elmer, Waltham, USA) was used to perform the elemental analysis.

Crystal structure determination and refinement. X-ray diffraction data of the hydrated $DAPH^+Cl^-$ were collected using a Rigaku XtaLAB Mini diffractometer equipped with Mercury 375R (2 × 2 bin mode) CCD detector. The data were collected with a graphite monochromated Mo-Kα radiation (λ = 0.71073 Å) at 296 K using ω scans. The data were reduced using CrysAlisPro 1.171.39.7f[35], and the space group determination was done using Olex2. The structure was resolved by the dual space method using SHELXT-2015[36] and refined by full-matrix least-squares procedures using the SHELXL-2015[37] software package through the OLEX2 suite[38].

Hirshfeld surface analysis and energy framework analysis. The intermolecular interactions in the $DAPH^+Cl^-$ has been studied and visualized by Hirshfeld surface (HS) analyses with Crystal Explorer 21.2[39,40]. The crystallographic information file of $DAPH^+Cl^-$ was used as an input file in 21.2 Crystal Explorer (Turner et al., 2017, Mackenzie et al., 2017). Various intermolecular interaction energies were calculated for the energy-framework analysis to get insights about different interaction energies involved in stabilizing crystal structure. The energy-framework analysis is a graphical representation of all the stabilizing energy components, e.g. electronic energy, dispersive energy, coulombic energy, total energy, etc., joined as cylinders of various colours between the centroids of the interacting pairs of molecules. It has been illustrated that the strength and contribution of a definite energy component are proportional to the radius of corresponding cylinders joining the molecules. We set the cylindrical radii to a scale factor of 25 and a cut-off value of 0 kJ/mol to visualize the interaction cylinders properly and identify the predominant interaction energy. A single-point wavefunction using the Hartree–Fock method with a 3-21G basis set at a cluster radius of 3.8 Å was generated around the target molecule, and an energy calculation was performed. Proper disorder modelling was done before performing Hirshfeld Surface analysis, and incomplete fragments are removed for computing energy calculation. The interaction energy is broken down as $E_{tot} = k_{ele}E'_{ele} + k_{pol}E'_{pol} + k_{disp}E'_{disp} + k_{rep}E'_{rep}$. The k values are scale factors for benchmarked energy models, $E'_{ele}$is the electrostatic energy, E'_{pol} is the polarisation energy, E'_{disp} is the dispersion energy, and E'_{rep} is the repulsive energy.

Bactericidal studies of the $DAPH^+Cl^-$ compound. *Clinical microbial cultures and culture media.* The antibacterial activity of $DAPH^+Cl^-$ was examined against clinical *Streptococcus pneumoniae, Escherichia coli* and *K. pneumonia.* The testing bacterial cultures (clinical cultures) were obtained from a clinical microbiological laboratory, Coimbatore, Tamil Nadu. Muller-Hinton agar media of Himedia Pvt. Himedia sterile discs and Himedia antibiotics disc (Tetracycline, 30 µg), Bombay, India, were used to prepare the media for studying the microbial test. The antibacterial activity of the $DAPH^+Cl^-$ was evaluated by employing a Himedia zone reader.

Inoculums and disc preparation. A 100 µL clinical bacterial species, *Streptococcus pneumoniae, Escherichia coli and K. pneumoniae* were inoculated individually in 5 mL of sterile nutrient broth (NB) media and incubated at 37 °C for 24 h. 200 µL from the stock culture was dispensed into 30 mL of sterile nutrient broth and incubated for 24 h to standardize the bacterial culture to 10^8 CFU/ml (colony forming units).

200 µg of the $DAPH^+Cl^-$ was dissolved in 100 µL sterile water to prepare the stock solution. 50 µL of diluted sample solution from the stock solution was added to Himedia sterile discs under aseptic conditions. Discs were air-dried thoroughly under aseptic conditions and used for the investigation of antibacterial activity.

Disc diffusion method (Kirby–Bauer method). The antibacterial activity of $DAPH^{+}Cl^{-}$ and the standard antibiotic, tetracycline, were evaluated following the disc diffusion method. The standardized inoculums (*Streptococcus pneumoniae, Escherichia coli, and Klebsiella pneumoniae*) were inoculated on the Mueller Hinton agar plates using sterile cotton swabs. The compound $DAPH^{+}Cl^{-}$ and tetracycline were added to the discs and placed on agar under aseptic conditions. Agar plates were incubated for 30 min at the refrigerator to diffuse the formulation into the agar, and finally, the plates were incubated at 37˚C for 24 h. Afterwards, the inhibition zone developed by the $DAPH^{+}Cl^{-}$ was measured with the Himedia zone reader.

In vitro SARS-COV-2 antiviral activity of the $DAPH^{+}Cl^{-}$. *Cytotoxicity assay against 1 × 10e4VeroE6 cells.* The cytotoxicity assay of the synthetic compound $DAPH^{+}Cl^{-}$ was performed in a 96-well plate format in a dose-dependent manner[41]. 1 × 10e4 VeroE6 cells were plated per well and incubated at 37 °C in a humidified 5% CO_2 for overnight to develop the monolayer formation. After 24 h, 10 µM remdesivir and three different concentrations of the $DAPH^{+}Cl^{-}$ (12 µM, 1.2 µM, 0.60 µM) and DMSO were added, and the plates were incubated for 30 h at 37 °C in a humidified 5% CO_2 (Vatansever et al., 2021 and Zhou et al., 2021). After removal of the cell supernatant, treated cells were stained with Hoechst 33,342 and Sytox orange dye. The images were taken at 10×, 16 photos per well, which covered 90% of the well area using ImageXpress Microconfocal molecular devices. Hoechst 33,342 nucleic acid stain is a popular cell-permeant nuclear counterstain that emits blue fluorescence when bound to ds-DNA. It stains all the live and dead cells. Sytox orange dye helps to stain the nucleic acids in cells with compromised membranes. This stain is an indicator of cell death. First, the software counted the total number of cells in the Hoechst image. The Sytox image was counted among Hoechst positive cells to determine the number of positive cells for sytox.

Immunofluorescence assay (IFA). The anti-SARS-CoV-2 assay was carried out in a 96 well plate format in which three wells were used for a sample of three different concentrations as previously described by Vernaite et al. 1×10^{4}VeroE6 cells were plated per well and incubated at 37 °C in a humidified 5% CO_2 for 24 h to form a monolayer. In the next day, 10 µM remdesivir and three different concentrations of the $DAPH^{+}Cl^{-}$ (12 µM, 1.2 µM, 0.60 µM) were added to the cells, and the plates were incubated for 30 h at 37 °C in a humidified 5% CO_2 (Vatansever et al., 2021 and Zhou et al., 2021). The normal VeroE6 cells without $DAPH^{+}Cl^{-}$ were considered as a control, while the remdesivir was used as a standard drug used for SARS-CoV-2 treatment as well as to make a comparison of the efficacy of the synthesized phenazinium chloride with remdesivir. The cells were infected with SARS-CoV-2 at an MOI of 0.1 and incubated at 37 °C in a humidified 5% CO_2 for 30 h. After 30 h, the cells were fixed in 4% paraformaldehyde. Afterwards, the cells were permeabilized with 0.3% tween-20 and stained with primary and secondary antibodies. The primary antibody-SARS-CoV2 nucleocapsid was the mouse monoclonal antibody (Catalog Number: 40143-MM05) and the secondary antibody was the anti-mouse alexafluor 568. The Hoechst 33,342 stain was used for staining the nucleus. Images were captured and analyzed using ImageXpress Microconfocal devices. The SARS-CoV2 nucleocapsid (Alexa flour-568) and Hoechst nuclei stain images were captured at 10×, 16 photos per well, covering 85% of the well area. The nucleocapsid positive cells and total nuclei were counted and compared with the control through MetaXpress software using a multi-wavelength cell scoring module.

Molecular docking studies, ADME and molecular property prediction. The rationale behind this study is to throw the light on the binding propensities of the hydrated 2,3-diaminophenazinium chloride with main protease (M^{pro}) and non-structural (nsp2 and nsp7-nsp8) proteins of SARS-CoV-2. Before the docking study with 2,3-diaminophenazinium chloride, the CIF files of the receptors were fetched from the protein data bank as M^{pro} (PDB ID: 6LU7), nsp2 (PDB ID: 7MSX) and nsp7-nsp8 (PDB ID: 6YHU). Before performing molecular interaction studies, M^{pro}, nsp2 and nsp7-nsp8 receptors were further curated for missing side-chain residues using What If interface (https://swift.cmbi.umcn.nl/servers/html/index.html). Molecular docking studies were performed with Autodock v 4.2.6.

Preparation of the ligand and receptors. The receptors and $DAPH^{+}Cl^{-}$ were prepared by adding polar hydrogen bonds followed by Kollman charge and Gastegier charges. The binding cavity for the $DAPH^{+}Cl^{-}$ docking in M^{pro}, nsp2 and nsp7-nsp8 were determined from the predefined co-crystallized X-ray structure from RCSB PDB. The residue positions were calculated within 3 Å space from the co-crystallized ligand. After the cavity selection in each case, the co-crystallized ligands were removed using the Chimera tool (https://www.cgl.ucsf.edu/chimera/) and subsequently, energy was minimized using the steepest descent and conjugate gradient algorithm. Then finally, merging the nonpolar hydrogens, both receptor and target compound were saved in pdbqt format.

Creating a simulation box. A grid box was created with parameters X = 68, Y = 58, and Z = 64 Å for 6LU7, X = 56, Y = 78, and Z = 61 for 7MSX and X = 108, Y = 78, and Z = 86 for 6YHU with 0.3 Å spacing. Following the Lamarckian Genetic Algorithm (LGA), docking studies of the protein–ligand complex were performed to achieve the lowest free energy of binding (ΔG).

Validation of docking parameters. During molecular docking studies, three replicates were performed. The total number of solutions was computed 50 in each case, with population size 500, the number of evaluations 2,500,000, the maximum number of generations 27,000, and the rest the default parameters were allowed. After docking, the RMSD clustering maps were obtained by reclustering commands with a clustering tolerance of 0.25 Å, 0.5 Å and 1 Å, respectively, to get the best cluster with the lowest energy score with a high number of

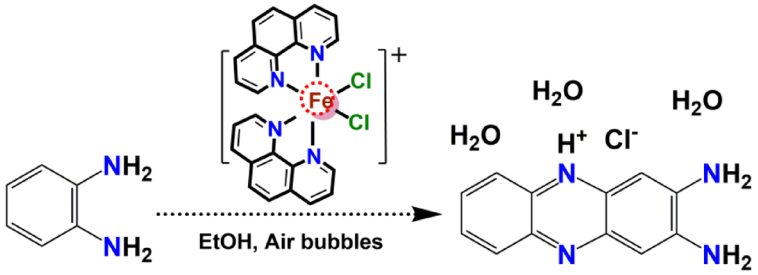

Figure 3. Synthetic route for hydrated diaminophenazinium chloride.

populations. The Ki values were determined from the free energy of binding energy using the present algorithm in Autodock 4.2.6. Lipinski's "Rule of five" was predicted by theoretical in silico ADME calculations[42]. A web tool of Swiss ADME was used to predict Lipinski's parameters[43]. Addition information related to the details of the molecular docking procedures is furnished provided in supporting information file.

Molecular dynamics (MD) simulation and molecular mechanics generalized born surface area (MM/GBSA) calculations. The MD simulations and MM-GBSA calculations were performed for 100 ns in triplicate to reveal the nature of interactions between DAPH$^+$Cl$^-$ and main protease, M^{pro} (PDB ID: 6LU7), non-structural proteins nsp2 (PDB ID: 7MSX), and nsp7-nsp8 (PDB ID: 6YHU) using the Desmond 2020.1 from Schrödinger, LLC. The OPLS-2005 force field[44–46] and explicit solvent model with the SPC water molecules were used in this system[47]. Na^+ ions were added to neutralize the charge. 0.15 M, NaCl solutions were added to the system to simulate the physiological environment. The NPT ensemble was set up using the Nose–Hoover chain coupling scheme[48] with temperature 27 °C, the relaxation time of 1.0 ps and pressure 1 bar maintained in all the simulations. A time step of 2 fs was used. The Martyna-Tuckerman–Klein chain coupling scheme[49] barostat method was used for pressure control with a relaxation time of 2 ps. The particle mesh Ewald method[50] was used for calculating long-range electrostatic interactions, and the radius for the coulomb interactions was fixed at 9 Å. RESPA integrator was used to calculate the non-bonded forces. The root mean square deviation (RMSD) was employed to monitor the stability of the MD simulations.

The binding free energy (ΔG_{bind}) of the protein–ligand complexes during MD simulation of the proteins with the DAPH$^+$Cl$^-$ was estimated using MM/GBSA module at the (Schrodinger suite, LLC, New York, NY, 2017-4). The OPLS 2005 force field, VSGB solvent model, and rotamer search algorithms were used to define the binding free energy during the calculation (Wang et al., 2018). The MD trajectories frames were selected at each 10 ns interval after MD run. The following formula was used to calculate the total free energy binding:

$$\Delta G_{bind} = G_{complex} - (G_{protein} + G_{ligand}) \quad (1)$$

where ΔG_{bind} = binding free energy, $G_{complex}$ = free energy of the complex, $G_{protein}$ = free energy of the target protein, and G_{ligand} = free energy of the ligand. The MMGBSA outcome trajectories were analyzed further for post dynamics structure modifications. Further, for all the 1000 frames of 100 ns MD simulations, the role of non-covalent interactions were estimated in MM/GBSA and plotted in 3D contour. Addition information related to the details of the methods of MD simulations is furnished in supporting information file.

Results and discussion

Synthesis and spectroscopic characteristics of DAPH$^+$Cl$^-$. The DAPH$^+$Cl$^-$ compound was synthesized through a direct catalytic oxidative coupling of o-phenylenediamine with ethanol's previously reported mononuclear iron(III) complex. The reaction was carried out in a 1:10 mol ratio of the iron complex: OPD and purging of 300 air bubbles were required to complete the catalytic oxidation of OPD. The synthetic procedure is shown in Fig. 3.

This structural characteristics and formulation of the DAPH$^+$Cl$^-$ compound was determined with FT-IR, UV–Vis and ^{1}H NMR spectral analysis. FT-IR spectrum of the DAPH$^+$Cl$^-$ exhibits important characteristics peaks at 3412 (very broad), 3149, 1624 and others (Fig. S1). The characteristic broad band in 3300–3500 cm^{-1} appeared for multiple aqua molecules' O–H stretching frequencies. The important peaks in the region 3300–3350 cm^{-1} and 3184 cm^{-1} attribute to the presence of -NH_2 groups. It is noticeable that the –NH and –OH stretching frequencies get merged in that region. The characteristic peak at 1624 cm^{-1} is assignable to the azomethine stretching vibration, respectively. These IR spectral data are in well concordance with the previously reported data.[51] The UV–Vis spectrum of DAPH$^+$Cl$^-$ in ethanol medium exhibits a high-intensity absorbance band at 258 nm and a moderate intensity electronic transition at 426 nm (Fig. S2). The electronic bands may be corroborated to the $\pi \rightarrow \pi^*$ and $n \rightarrow \pi^*$ electronic transitions of DAPH$^+$Cl$^-$ (Fig. S2). This observation is in high agreement with the previously reported data of the phenazine produced through ferric chloride and some structurally related compounds[52–54]. The ^{1}H NMR spectrum of DAPH$^+$Cl$^-$ defines the protons' location in DAPH$^+$Cl$^-$ (Fig. S3). The singlet signals at 11.66 and 10.99 ppm represent the indole-NH protons in DAPH$^+$Cl$^-$. The methylene protons of DAPH$^+$Cl$^-$ were also detected and confirmed from the appearance of the signal at 5.82 ppm. The entire protons rise in the region from 8.33 to 6.81 ppm can be assignable to the presence of aromatic protons in DAPH$^+$Cl$^-$ and agree well with the previously reported data[51,52].

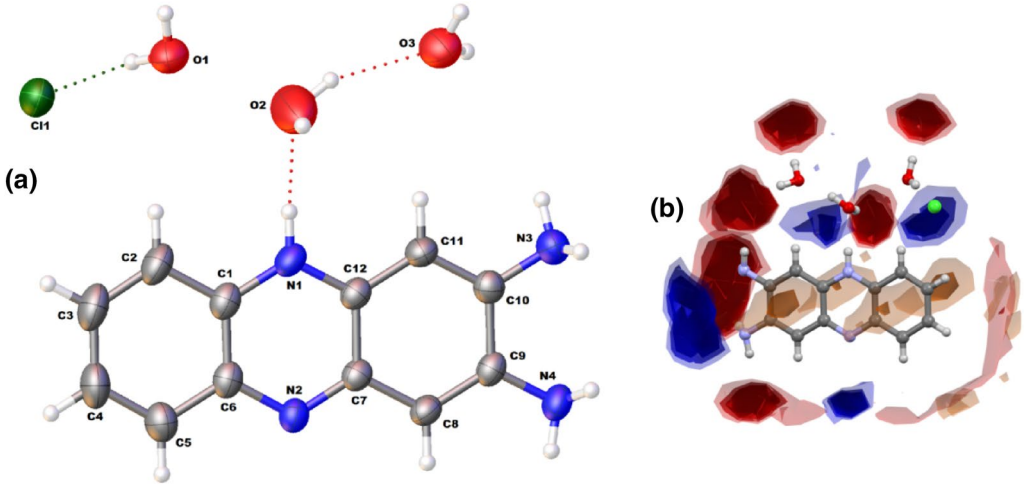

Figure 4. (**a**) An ORTEP diagram of the hydrated $DAPH^+Cl^-$ with 30% probability; (**b**) Interaction map of $DAPH^+Cl^-$ showing the suitability of interactions adopting the intensified red and blue regions.

Parameters	$DAPH^+Cl^-$
Empirical formula	$C_{12}H_{17}N_4ClO_3$
Formula weight	300.75
Temperature (K)	296
Crystal system	Monoclinic
Space group	$P\bar{1}$
a (Å)	6.8028(11)
b (Å)	9.8872(16)
c (Å)	11.2737(19)
Volume ($Å^3$)	713.2(2)
Z	2
ρ ($gcm+^3$)	1.401
μ (mm^{-1})	0.281
F (000)	316
R_{int}	0.015
θ ranges (°)	2.0–24.7
Number of unique reflections	2897
Total number of reflections	5348
Final R indices	0.0620, 0.1916
Largest peak and hole ($eÅ^{-3}$)	0.51 and − 0.48

Table 1. Crystallographic data and structure refinement parameters for hydrated $DAPH^+Cl^-$.

Crystal structure, Hirshfeld surface analysis, crystal engineering perspective and energy frameworks. The single crystals of the oxidation product, 2,3-diaminophenazine (DAP) in its chloride salt, were obtained in catalytic OPD oxidation with the reported iron(III) complex. The crystal structure analysis of $DAPH^+Cl^-$ reveals that the compound crystallizes in a triclinic crystal system with a *P*-1 space group. An ORTEP view of $DAPH^+Cl^-$ is shown in Fig. 4a. The X-ray structure of $DAPH^+Cl^-$ displays an oxidative fusion of two OPD molecules with highly planar aromatic centroids. It is further observed that one of the nitrogen atoms (N1) in the middle aromatic centroid gets protonated, and the cationic charge is counterbalanced with the chloride ion. The crystallographic refining parameters for $DAPH^+Cl^-$ are also given in Table 1. Selected bond distance and bond angles of the compound are shown in Table S1. Further, three water molecules co-exist as solvate molecules with $DAPH^+Cl^-$ and helps the molecular system to get stabilized in the crystalline phase. The generated interaction landscape of $DAPH^+Cl^-$ has been depicted from its 3D coordinates (Fig. 4b).

The interaction map exhibits the interaction preferences by highlighting regions around the molecule (maps) where chemical functional groups (probes) are likely to contact. Full Interaction maps are instrumental in highlighting the potentiality and understanding the interaction patterns between a ligand and a protein. The red and blue areas in the maps denote the regions in which there is a high probability of locating a hydrogen bond acceptor and H-bond donor, respectively. The brown spots in the map indicate the hydrophobic preferences.

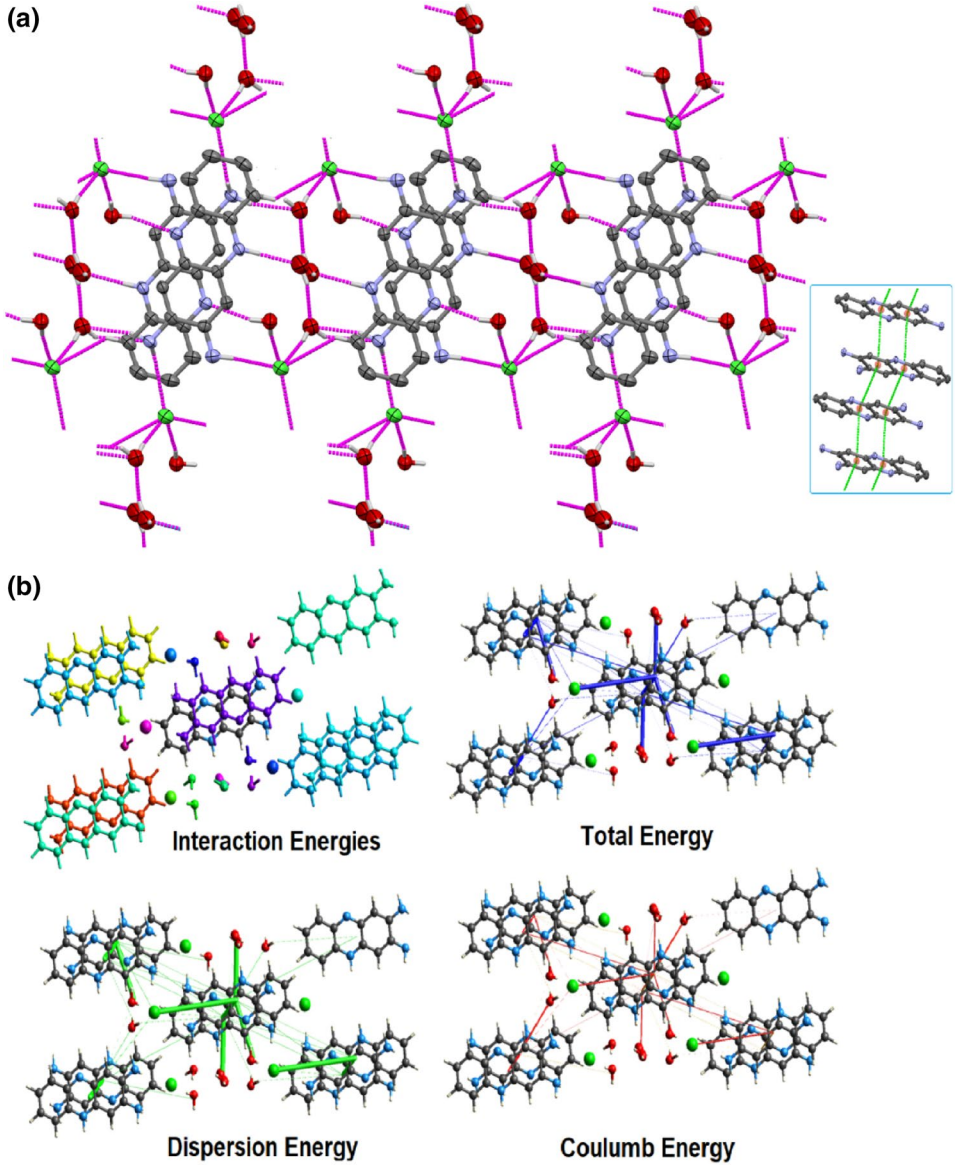

Figure 5. (**a**) Formation of a unique type of $(H_2O)_2\ldots Cl^-\ldots(H_2O)$ cluster throng strong H…Cl, H…O and H…N interactions and its effect for the construction of supramolecular architecture in $DAPH^+Cl^-$ along *bc* plane; Inset: π…π interactions of AB…AB type (inset); (**b**) Interaction energies participating in the crystal of $DAPH^+Cl^-$ to develop the supramolecular framework.

Indeed, the observed intensified blue and red landscape around the hydrated $DAPH^+Cl^-$ suggests the worth of attention for its potential candidature against different microbial species (Fig. 4b).

In the asymmetric unit of $DAPH^+Cl^-$, two of the three crystallized water molecules form strong H-bonding with each other and with the protonated-N of $DAPH^+Cl^-$. Besides this, one crystallizes water interacts with a chloride ion with strong H-bonding in the asymmetric unit. Analysis of the self-assembled architecture for $DAPH^+Cl^-$ suggests that a beautiful $(H_2O)_2\ldots Cl^-\ldots(H_2O)$ cluster is formed in *bc* plane and displayed in Fig. 5a. This solvent-anion cluster remains an important binder between two cross-linked dimeric DAP units of opposite orientation. The opposite direction of the molecules are further stabilized through strong π…π interactions among the aromatic centroids of dpa and developed AB…AB type of layer in the crystalline phase (Fig. 5a). Notably, the water molecules and chloride ions form an attractive water-chloride cluster. The hydrogen bonding interaction distances were found very strong, starting from 1.89 to 2.38 Å. The intermolecular interaction parameters are given in Table S2.

Moreover, the computational results on the interaction energy frameworks for $DAPH^+Cl^-$ were examined. The interaction energies involved in growing supramolecular framework followed by graphical representation of individual interaction energy components is shown in Fig. 5b. The details of interaction energies are summarized in Table S3. The molecular pair-wise contribution of energies is evaluated, followed by the sum of individual energy components multiplied by scale factor, which furnished the total interaction energy of the

crystal. The total interaction energies are electrostatic (E'_{ele} = −91.3 kJ/mol), polarization (E'_{pol} = −77.4 kJ/mol), dispersion (E'_{disp} = −486.4 kJ/mol), repulsion (E'_{rep} = 264.8 kJ/mol), and total interaction energy (E_{tot}) was calculated as −366.92 kJ/mol (Fig. 5b). Hence, the supramolecular architecture is highly stable with total interaction energy of −366.92 kJ/mol and dispersive energy interactions dominate the framework.

The Hirshfeld surface analysis was further studied for $DAPH^+Cl^-$ to reveal the binding fate of the chloride ion for the stabilization of $DAPH^+$ species. The Hirshfeld surface was examined over a definite d_{norm} (− 0.7308 to 1.1993 a.u.) and a view of Hirshfeld surfaces of $DAPH^+Cl^-$ mapped over d_{norm}, shape index, curvedness and fragment patch is shown in Fig. S4. The surface over a definite d_{norm} showed a wide area of multiple red spots, which suggests the presence of strong to very strong H…Cl and H…O interactions (Fig. S4). The surface mapped over shape index ranging − 1.00 to + 1.00 a.u. for $DAPH^+Cl^-$ exhibited intense red and blue spots, ensuring the presence of H…Cl and H…O and weak π…π/C-H…π interactions among the dpa units (Fig. 5a). In addition, 2D fingerprints (Fig. S5) plots were also calculated (Table S4), which displayed the active involvement of the H-bonded and π…π interactions in the crystalline phase.

Bactericidal activity of $DAPH^+Cl^-$. The bactericidal activity of the hydrated $DAPH^+Cl^-$ was studied against the clinical bacterial species *Streptococcus Pneumoniae, Escherichia coli* and *K. pneumoniae* following a disc diffusion method. The results of the inhibition zone diameters are shown in Fig. S6 and tabulated in Table S5. The minimum inhibitory concentration (MIC) values were estimated for $DAPH^+Cl^-$ and tetracycline under identical experimental conditions against *Streptococcus Pneumoniae* to understand the potency of the antibacterial efficiency. The MIC values were determined as 32.5 µg/mL for $DAPH^+Cl^-$ and 29.0 µg/mL for tetracycline. The comparable MIC value of $DAPH^+Cl^-$ with respect to tetracycline certainly recommends the competent inhibition activities of $DAPH^+Cl^-$ against the growth of bacterial species.

Furthermore, transmission electron microscope images were recorded on the *Streptococcus Pneumoniae* bacterial cells isolated from the MIC. The isolated bacterial cells were sputter-coated with a thin layer of gold and observed under a scanning electron microscope. The TEM images of the $DAPH^+Cl^-$ treated bacterial cells and $DAPH^+Cl^-$ untreated control bacterial cells are shown in Fig. S7. The electron microscope scanning images showed the wrinkling of the bacterial cells and portrayed the destruction of the cell membrane of *Streptococcus Pneumoniae* bacterial.

In vitro *SARS-COV-2 screening activity of $DAPH^+Cl^-$.* *Cytotoxicity of the $DAPH^+Cl^-$.* Cell viability and cell toxicity assays are significant for assessing the cellular responses to a tested compound during its screening activity in a biological experiment. Typically, cell viability assay provides an important readout of healthy cells by measuring the metabolic activity or cell proliferation[55]. Cell viability, which measures the proportion of live and healthy cells within a total cell population, can also be estimated by cell toxicity assay through examining cell growth replication. The cytotoxicity of the $DAPH^+Cl^-$ and remdesivir was evaluated independently against 1 × 10e4VeroE6 cells (n = 3) in a dose-dependent manner. The non-cytotoxic concentration was also determined for $DAPH^+Cl^-$ and remdesivir under a similar experimental condition. It is observed that the compounds exhibit a non-cytotoxic concentration against 1 × 10e4VeroE6 cells up to a dose of 12 µM and 10 µM for $DAPH^+Cl^-$ and remdesivir, respectively.

Further, the percentage cell viability of the compounds was also estimated for 1 × 10e4VeroE6 cells (Fig. S8). Compared to the control, the percentage cell viability of the 1 × 10e4VeroE6 cells were determined as 87.3, 97.3, 88.5% at a 0.6, 1.2, 12 µM concentration for $DAPH^+Cl^-$ while 99.23% cell viability was displayed by remdesivir at 10 µM (Table S6). The cytotoxic effect of $DAPH^+Cl^-$ and remdesivir on 1 × 10e4VeroE6 cells is shown in Fig. 6a-d. Therefore, the high percentage of cell viability at a non-cytotoxic concentration of $DAPH^+Cl^-$ against 1 × 10e4VeroE6 cells makes a great promise to develop a potential therapeutic for SARS-CoV-2 under the gravity of present the pandemic.

Antiviral efficacy of $DAPH^+Cl^-$ and remdesivir following immunofluorescence assay. The in vitro antiviral activities of the synthetic $DAPH^+Cl^-$ and remdesivir at non-cytotoxic concentrations were further evaluated through immunofluorescence assay (IFA) against VeroE6 cells to understand the viral screening efficacy. It is well documented that remdesivir is a globally prescribed antiviral therapeutic agent for treating SARS-CoV-2, and a comparison of the antiviral activity for $DAPH^+Cl^-$ and remdesivir may put some ray of hope in this context. The anti-SARS-CoV-2 activity was further quantified using primary (mouse monoclonal antibody) and secondary antibodies (anti-mouse alexafluor 568) using IFA (Table S6). 10 µM of remdesivir can significantly inhibit 99.1% of the SARS-CoV-2 infection (Fig. 61b) while DMSO (Dimethyl sulfoxide) as a control didn't exhibit any inhibition (Fig. 61d). $DAPH^+Cl^-$ at 0.6 µM and 1.2 µM didn't display any inhibition towards the replication of SARS-CoV-2. However, $DAPH^+Cl^-$ is very effective, as evident from its 70% inhibition activity at 12 µM (Fig. 61a). The uninfected VeroE6 cells are shown in Fig. 61c. Most probably, with the increase of the concentration of $DAPH^+Cl^-$, a cause of substantial interaction with the main protease proteins ceases the replication of RNA genome and result in the prevention of viral attachment to the cells was observed[56]. However, detailed mechanistic research needs to be studied to bring a more scientific vision in this context.

Molecular docking studies. Molecular docking studies were performed to decipher the binding propensities of $DAPH^+Cl^-$ with the main protease (M^{pro}) and non-structural proteins (nsp2 and nsp7-nsp8) of SARS-CoV-2. The images of docked complexes, molecular surfaces, 3D and 2D interactive plots for $DAPH^+Cl^-$ with the proteins of SARS-CoV-2 are shown in Fig. 7. To evaluate the binding interaction between hydrated $DAPH^+Cl^-$ and M^{pro}, the best binding pose was obtained from the best RMSD cluster having 0.25 Å tolerances containing 75% population in the same cluster. The $DAPH^+Cl^-$ showed considerable hydrogen bonding interactions with the

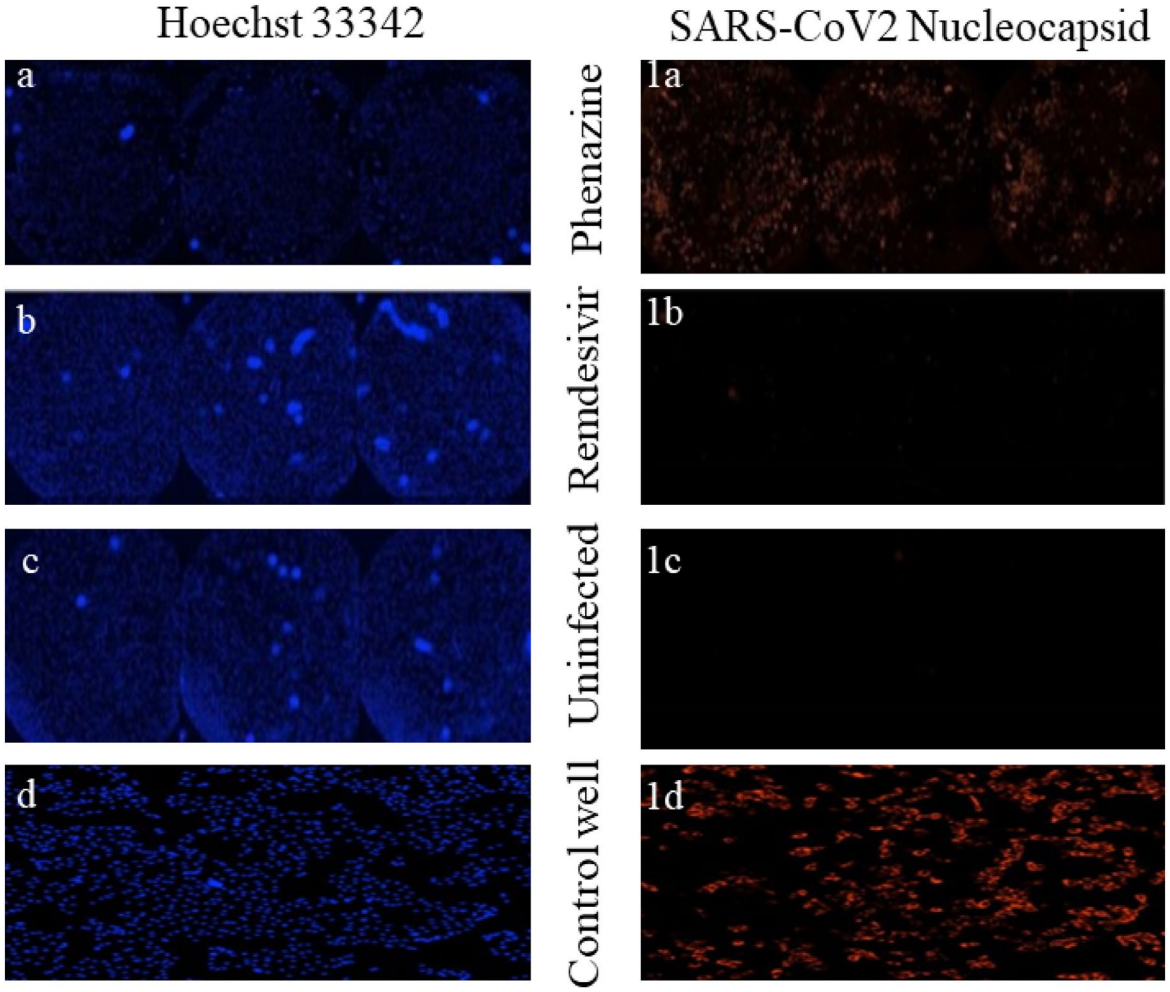

Figure 6. Representative morphological changes were observed in 1 × 10e4VeroE6 cells at the non-cytotoxic concentration of $DAPH^+Cl^-$ and remdesivir as revealed in Hoechst33342 staining (left) and nucleocapsid staining (right). [**a** to **a1**: VeroE6 cells infected virus treated with $DAPH^+Cl^-$; **b** to **b1**: VeroE6 cells infected virus treated with remdesivir; **c** to **c1**: uninfected VeroE6 cells; d to d1: virus infected VeroE6 cells].

amino acids Arg188, Thr190 and Glu166 of M^{pro} along with vdw and π…π interactions (Fig. 7A). The effective change of free energy for binding of $DAPH^+Cl^-$ with M^{pro} was estimated as ΔG = –6.66 kcal/mol with predictive inhibition concentration, Ki = 13.11 μM.

The binding interaction of $DAPH^+Cl^-$ with the binding pocket of the non-structural protein, nsp2 showed a substantial binding effect through intermolecular hydrogen bonding, vdw and C…π interactions. Here, the best binding pose was obtained from the best RMSD cluster having 0.25 Å tolerances contain 95% population in the same cluster. The amino acid, Cys72 binds $DAPH^+Cl^-$ with intermolecular hydrogen bonding. However, other non-covalent interactions like vdw forces and C…π interactions were effectively dominant in the binding of DAPH + Cl- with the nsp2 site (Fig. 7B). The change of free energy for binding of $DAPH^+Cl^-$ with nsp2 was noteworthy as ΔG = – 7.91 kcal/mol and Ki = 7.44 μM (Fig. 7B).

Furthermore, the binding effect of $DAPH^+Cl^-$ with nsp7-nps8 was also evaluated and displayed in Fig. 7C. In this binding, the best binding pose was obtained from the best RMSD cluster having 0.25 Å tolerances contain 78% population in the same cluster. It is evident from Fig. 7C that $DAPH^+Cl^-$ compound binds with nsp7-nsp8 through hydrogen bonding, vdw forces, π-sigma and π-alkyl interactions. The change of binding energy of $DAPH^+Cl^-$ with nsp7-nsp-8 was found to be – 7.12 kcal/mol with predictive Ki, 8.61 μM. The details of the interaction between $DAPH^+Cl^-$ and M^{pro}, as well as nsp7-nsp8 proteins, are summarized in Table S7.

The molecular docking studies of $DAPH^+Cl^-$ with main protease and non-structural proteins of SARS-CoV-2 suggest that $DAPH^+Cl^-$ displays a good binding propensity with nsp2 protein compared to nsp7-nsp8 and M^{pro} of SARS-CoV-2. The change of free energy for binding of $DAPH^+Cl^-$ with nsp2, nsp7-nsp8 and M^{pro}, and Ki values further ensure the predictability for the priority of binding (Table S7). Noteworthy, the structural features of M^{pro}, nsp2 and nsp7-nsp8 are entirely different. The predictability of binding through molecular docking does not correlate with the binding priority among the different $DAPH^+Cl^-$ bound protein complexes. However, the negative values for the changes of free energy for binding of DAPH+Cl^- with different proteins of SARS-CoV-2 strongly recommend a considerable binding propensity of $DAPH^+Cl^-$ with the proteins. Nevertheless, the tested drug-like nature of $DAPH^+Cl^-$ against SARS-CoV-2 was also proved by calculating ADME values (Table S8).

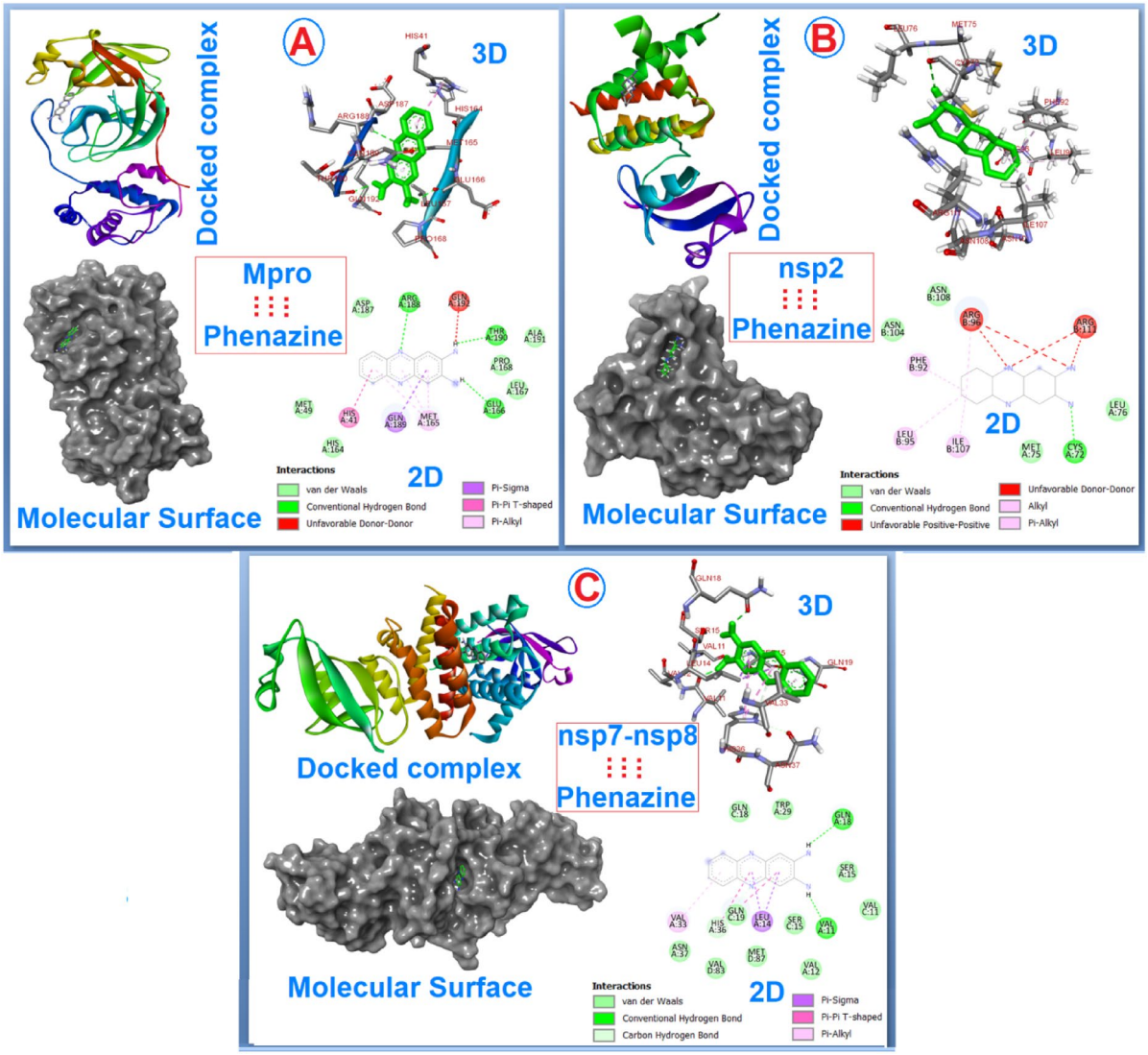

Figure 7. (**A**) Binding motifs of $DAPH^{+}Cl^{-}$ with the active sites of M^{pro} along with 2D and 3D modeled interactive plots showing various non-covalent interactions; (**B**) Binding motifs of $DAPH^{+}Cl^{-}$ with the binding sites of nsp2 including 2D and 3D modeled interactive plots based on different non-covalent interactions; (**C**) Binding motifs of $DAPH^{+}Cl^{-}$ with the binding sites of nsp7-nsp8 with 2D and 3D modeled interactive plots showing various non-covalent interactions.

The cytotoxic effect of $DAPH^{+}Cl^{-}$ was well recognized as passing Lipinski's "Rule of 5" with 0 violation which recommends the promising therapeutic behavior against SARS-CoV-2.

The molecular docking results are further corroborated with the earlier reported work[57,58]. Very recently, Hosseini and co-workers reported few potential inhibitors like Ramelteon, Levomefolic acid, Ketoprofen etc. against SARS-CoV-2, which displayed the binding energy ranging between − 6.0 and − 6.66 kcal/mol at the binding cavity of the M^{pro}[57]. In contrast, at the same binding cavity, $DAPH^{+}Cl^{-}$ displayed to have similar free energy of binding. It is also documented that minimal reports are available for nsp2 inhibition; therefore, the study envisaged here for nsp2 inhibition is a novel addition. Moreover, the inhibition of nsp7-nsp8 by $DAPH + Cl^{-}$ in this study corroborated the same binding site as reported for commercial antiviral drug darunavir with similar range of binding energy (Halder, 2021)[58].

MD simulation and MMGBSA calculations. Molecular dynamics (MD) simulation of the 2,3-diaminophenazinium bound main protease, (M^{pro}) and non-structural proteins (nsp2 and nsp7-nsp8) complexes of the SARS-CoV-2 were studied in detail to understand the nature of possible binding motifs and structurally stable conformations. Replication of the simulations was done in triplicate using the same system parameters to obtain the accurate information of structural convergence in MD studies. The root mean square deviation (RMSD) means a standard measure of structural distance between coordinates. It indicates the extent of structural deviation from its original conformation with time. The RMSD value is a measure of how much the protein conformation has changed with the progress of time. It is well established that increase in the RMSD plot with time, increases the deviation of the protein from its original conformation. The root mean square deviation (RMSD)

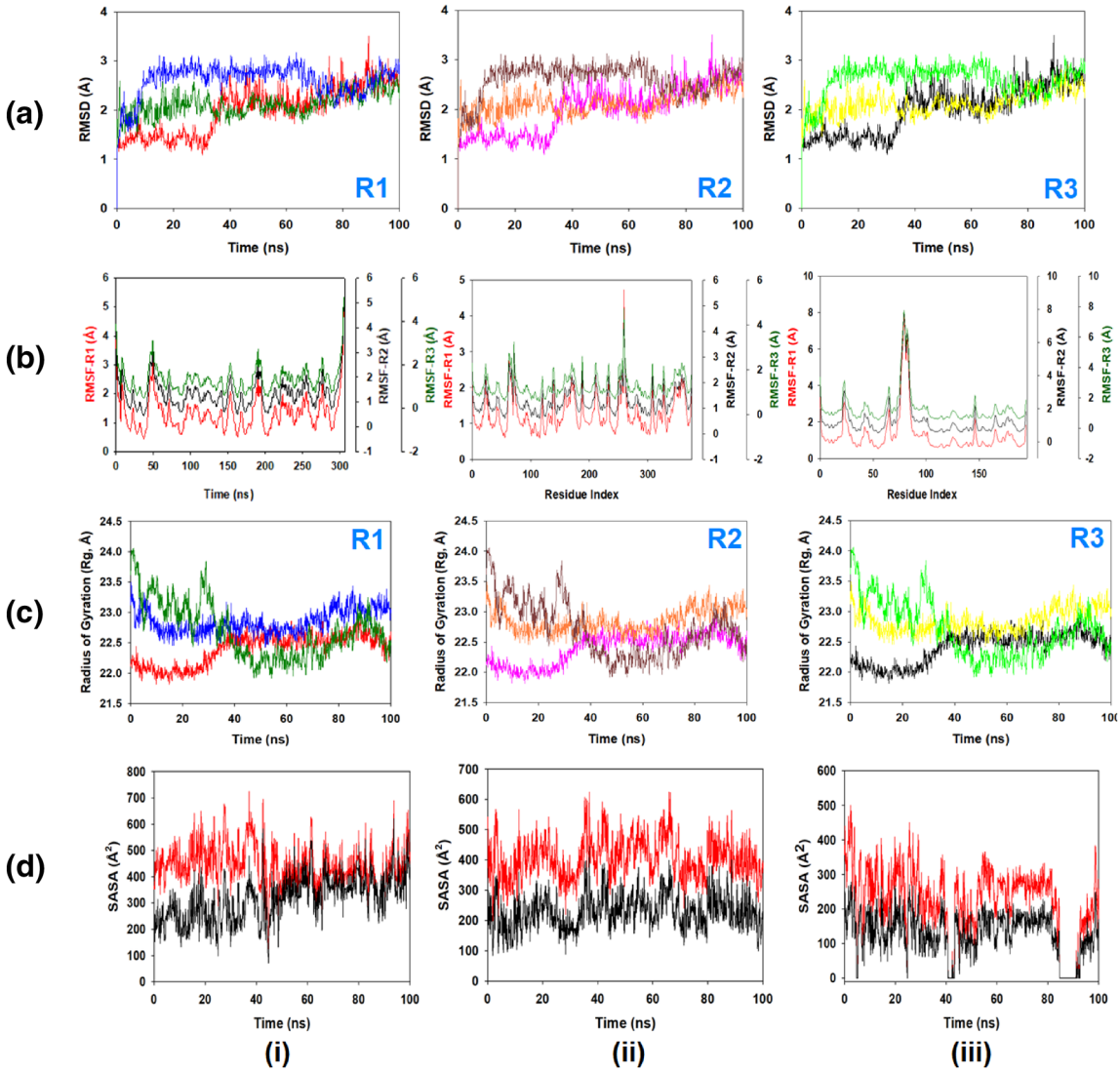

Figure 8. MD simulation trajectory analysis from 100 ns time frame in triplicate displayed (**A**) R1 (replicate 1) RMSD plots of DAPH^{+}Cl^{-} bound M^{pro} (red), nsp2 (green) and nsp7-nsp8 (blue), R2 (replicate 2) RMSD plots of DAPH^{+}Cl^{-} bound M^{pro} (purple), nsp2 (orange) and nsp7-nsp8 (dark red), R3 (replicate 3) RMSD plots of DAPH^{+}Cl^{-} bound M^{pro} (black), nsp2 (yellow) and nsp7-nsp8 (parrot green); (**B**) [Replicate (1, 2, 3), left panel]: RMSF plots of DAPH^{+}Cl^{-} bound M^{pro}, [replicate (1, 2, 3), middle panel]: RMSF plots of DAPH^{+}Cl^{-} bound nsp2, and [replicate (1, 2, 3), right panel]: RMSF plots of DAPH^{+}Cl^{-} bound nsp7-nsp8. The RMSF plots of three replicates coded color (red, R1), (black R2) and (green R3). The Y axis scales were adjusted to display the individual replicate plots; (**C**) R1 (replicate 1) Radius of gyration (Rg) plots of DAPH + Cl^{-} bound M^{pro} (red), nsp2 (green) and nsp7-nsp8 (blue), R2 (replicate 2) Radius of gyration (Rg) plots of DAPH^{+}Cl^{-} bound M^{pro} (purple), nsp2 (orange) and nsp7-nsp8 (dark red), R3 (replicate 3) Radius of gyration (Rg) plots of DAPH^{+}Cl^{-} bound M^{pro} (black), nsp2 (yellow) and nsp7-nsp8 (parrot green); (**D**) Binding SASA in the presence (black) and absence (red) of DAPH^{+}Cl^{-} with M^{pro} (left panel), nsp2 (middle panel) and nsp7-nsp8 (right panel). Lowering of SASA (black) signify the binding of ligand to the respective proteins.

of Cα-backbone atoms of the 100 ns MD simulation trajectories displayed vibrational deviations with 1.5 Å from beginning to end of the simulation, signifying a stable conformation of the DAPH^{+}Cl^{-} bound M^{pro} (Fig. 8A, red). The nsp2 bound complex with DAPH^{+}Cl^{-} showed a 0.5 Å displacement of the RMSD (Fig. 8A, green), while nsp7-nsp8 bound DAPH^{+}Cl^{-} displayed an overall 0.8 Å deviation (Fig. 8A, blue). In all three replicates, similar displacements were observed (Fig. 8A; R1, R2 and R3). It is evident that nsp2 proteins showed a minimum displacement of the average RMSD (0.5 Å) while the nsp7-nsp8 and M^{pro} displayed a relatively higher degree of average deviation of RMSD. RMSD less than < 1.5 Å for nsp2, nsp7-nsp8 and M^{pro} with respect to the true binding of DAPH^{+}Cl^{-} attributing to stable conformations of DAPH^{+}Cl^{-} bound complexes and a reasonable estimation of precise calculations of phenazine chloride-proteins interactions.

The root-mean-square fluctuation (RMSF) plot measures the average deviation of a protein residue over time from a reference position (typically the time-averaged position of the protein residue). Thus, RMSF analyzes the

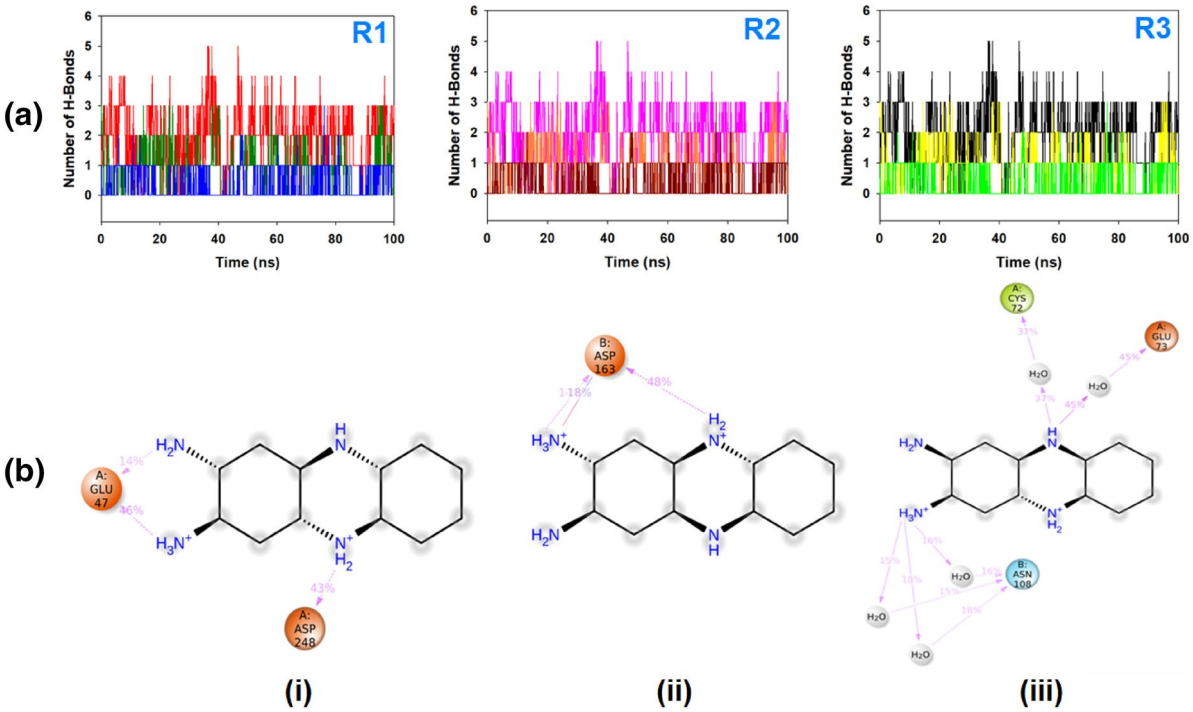

Figure 9. MD simulation trajectory analysis from 100 ns time frame in triplicate displayed (**A**) Number of hydrogen bonds formed between DAPH$^+$Cl$^-$ and proteins during 100 ns simulation R1 (replicate 1) M^{pro} (red), nsp2 (green) and nsp7-nsp8 (blue); R2 (replicate 2) M^{pro} (purple), nsp2 (orange) and nsp7-nsp8 (dark red) and R3 (replicate 3) M^{pro} (black), nsp2 (yellow) and nsp7-nsp8 (parrot green); (**B**) 2D interaction plot of DAPH$^+$Cl$^-$ with M^{pro} (left panel), nsp2 (middle panel) and nsp7-nsp8 (right panel) during 100 ns of simulation. Dotted (purple) lines indicate H-bonds, amino acid residues inside sphere and H_2O displaying water bridges.

portions of structure that are fluctuating from their mean structure the most (or least). It is also evident that lower RMSF values signify the structurally compact conformations while the higher RMSF values indicate more flexible loop regions. RMSF of the amino acid residue position of 100 ns simulation trajectories of DAPH$^+$Cl$^-$ bound proteins are displayed in Fig. 8B. All the data are measured in triplicates and the Y-axis is repositioned every time to show the individual run outcomes. The individual fluctuations of amino acid residues over a function of time from the reference structure (0 ns) after time 100 ns of the final structure of M^{pro} displayed residue positions 50 and 180 having significant fluctuations averaging 1.5 Å (Fig. 8B, left panel). However, no other important fluctuating residues were observed. While nsp2 bound to DAPH$^+$Cl$^-$ Cα backbone residues displayed considerable fluctuations at residue positions 70 (1.7 Å) and 260 (2.3 Å) (Fig. 8B, middle panel) and nsp-nsp8 showed at residue position 80 (3.5 Å) (Fig. 8B, right panel). From the average RMSF values of the proteins, it may be suggested that the non-structural proteins exhibited structurally flexible conformations while M^{pro} proteins showed a relatively more compact conformations. Typically, non-structural proteins exist in a more flexible conformation relative to main protease and the results are in well agreement with the natural structural flexibility of the proteins.

The radius of gyration (Rg) is defined as the distribution of atoms of a protein around its axis. The Rg plots were also determined as Rg accounts on the size and compactness of the protein in the ligand-bound state. Lower is the Rg score, higher is the compactness of the docked conformations. The Rg plots are displayed in Fig. 8C. The Rg plot of Cα-backbone indicates that nsp2 protein (Fig. 8C, blue) has a lowering of Rg values from 23.5 to 23.2 Å, meaning compactness with an average of 0.3 Å from the beginning to the end of 100 ns simulation. In contrast, the Rg score in nsp7-nsp8 protein was observed with 1.5 Å total alterations from beginning to end (Fig. 8C, green). However, the Rg plot of M^{pro} displayed deviations from very less significant lowering, thus indicating relatively less compactness of the structure with DAPH$^+$Cl$^-$ bound state (Fig. 8C, red) as compared to nsp2 and nsp7-nsp8 bound complex.

Followed by Rg analysis, similar patterns were also observed in solvent accessible surface area (SASA) analysis in both ligand-bound and unbound states. It is visible from Fig. 8D that in the unbound state of ligand M^{pro}, nsp2 and nsp7-nsp8 displayed high surface area accessible to solvent (Fig. 8D, (i), (ii), (iii), red) while binding with DAPH$^+$Cl$^-$, the SASA value lowered as compared to the unbound state (Fig. 8D, (i), (ii), (iii), black). This signifies the ligand DAPH$^+$Cl$^-$ binding compels the respective proteins to become more compact and less flexible. Similarly, Dash and co-workers reported the significance of SASA after ligand binding to the receptor[59].

The average hydrogen bonds formed between DAPH$^+$Cl$^-$ and the respective proteins during the 100 ns simulation were also noted and recorded in Fig. 9A. A limited number of hydrogen bonds are displayed in triplicate MD simulations of DAPH$^+$Cl$^-$ and M^{pro} (Fig. 61A,R1). Overall three hydrogen bonds were formed with Glu47 and Asp248 throughout the simulation and confirmed from 2D ligand binding plot (Fig. 9B, (i)). While, DAPH$^+$Cl$^-$ bound to nsp2 displayed a couple of hydrogen bonds formed with Asp163 residue throughout the simulation time (Fig. 9A, R2) and also confirmed in 2D interaction plot (Fig. 9B, (ii)). On the other hand,

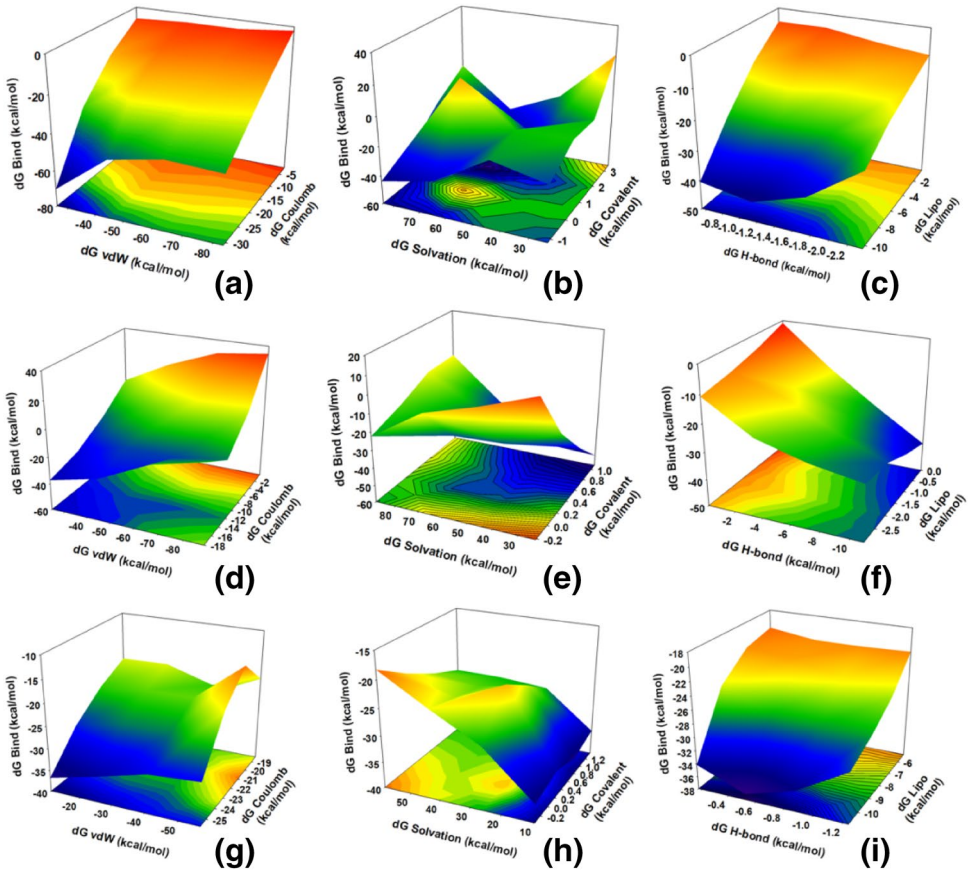

Figure 10. 3D contour plots (in sheets) of correlation of non-bonded interactions from MM/GBSA trajectory of 100 ns (all 1000 frames). The principal interacting van der waal's, coulomb, H-bond, Lipo, salvation and covalent energies are displayed and compared with dG Bind in kcal/mol. (**A**) nsp2 with $DAPH^+Cl^-$ displayed high binding energy due to a good correlation (blue region) of dG vdW and dG Coulomb, (**B**) lessening of binding energy due to negative correlation of dG salvation and dG covalent energies, (**C**) important correlation between dG Lipo and dG H-bond toward augmenting binding energy of nsp2-$DAPH^+Cl^-$ complex; (**D**) nsp-7-nsp8 with $DAPH^+Cl^-$ displayed good binding energy due to considerable correlation (blue region) of dG vdW and dG Coulomb, (**E**) lessening of binding energy due to negative correlation of dG salvation and dG covalent energies, (**F**) important correlation between dG Lipo and dG H-bond toward augmenting binding energy of nsp7-nsp8 $DAPH^+Cl^-$ complex; (**G**) M^{pro} with $DAPH^+Cl^-$ displayed high binding energy due to significant correlation (blue region) of dG vdW and dG Coulomb, (**H**) lessening of binding energy due to negative correlation of dG salvation and dG covalent energies, (**I**) considerable correlation between dG Lipo and dG H-bond toward augmenting binding energy of M^{pro}—$DAPH^+Cl^-$ complex. Sheet colour blue indicates the highest correlation, green moderate and yellow least.

nsp7-nsp8 displayed a noticeable number of hydrogen bond formation with $DAPH^+Cl^-$ (Fig. 9A, R3), and most of the interactions were directed by water bridges as shown in 2D interaction plot (Fig. 9B, (iii)). The existence of hydrogen bonds between proteins and $DAPH^+Cl^-$ has strengthened the binding, helping to make it more stable during the simulation.

Utilizing the 100 ns MD simulation trajectory of the last frame (100 ns), the binding free energy along with other contributing energy in the form of MM/GBSA was determined for $DAPH^+Cl^-$ complexed with M^{pro}, nsp2 and nsp7-nsp8. All the triplicate MD simulations were considered and standard deviation is calculated and represented with the binding energies. By considering all the 1000 frames of 100 ns MD simulation, the non-bonded interactions were measured in MM/GBSA and plotted in 3D contour. The binding free energy (dG Bind) of $DAPH^+Cl^-$ with nsp2 displayed -25.7 ± 0.1 kcal/mol. The results displayed in Fig. 10A-C, suggested that the maximum contribution to dG_{bind} in the simulated $DAPH^+Cl^-$ bound nsp2 complex stability through the contribution of dG_{bind} Coulomb, dG_{bind} vdW dG_{bind} H-bond and dG_{bind} Lipo. dG_{bind} Coulomb and dG_{bind} vdW attributed for better correlation in the making toward higher binding energy (Fig. 10A), similarly, dG_{bind} H-bond and dG_{bind} Lipo (Fig. 7C). However, contrasting behaviour showed by dG_{bind} covalent and dG_{bind} salvation energies lowered the binding energy (Fig. 10B). The overall binding free energies are the outcome of all these positive and negatively correlated interacting energies. The binding energy (dG_{bind}) of $DAPH^+Cl^-$ bound nsp7-nsp8 was found to be -24.5 ± 0.7 kcal/mol (Fig. 10D,E,F) and the trajectory analysis for the contribution of total binding free energies displayed a similar pattern of the phenomenon as in the case of nsp2. On the other hand, $DAPH^+Cl^-$ bound M^{pro} displayed dG Bind -19.2 ± 0.3 kcal/mol. The highest binding energies from every

10 ns of M^{pro} trajectories displayed the high contribution of coulombic energy (blue) and van der Wall's energy toward more negative free energy as (Fig. 10G) and Lipo energy as well as H-bonds energy (Fig. 10I). While solvation energy and covalent energies disturbed the system more toward destabilization with positive free energies (Fig. 10H). While comparing with the binding free energies obtained from docking results, the MM/GBSA energies can be comparable where nsp2, nsp7-nsp8 displayed greater binding as compared to M^{pro} with $DAPH^{+}Cl^{-}$.

Therefore, MM/GBSA binding energy analysis from the MD trajectories recommends that the diaminophenazinium salt shows a considerable binding effect of $DAPH^{+}Cl^{-}$ with M^{pro}, nsp2 and nsp7-nsp8 proteins, leading to stable conformations. Moreover, a positive correlation can be established from the MM/GBSA binding energies and predicted inhibitory concentration (Ki) obtained from the molecular docking studies. As the binding energies increased from M^{pro} to nsp7-nsp8 to nsp2, the Ki values decreased following a similar pattern. Therefore, it can be suggested that the lower the binding energy, low the concentration of $DAPH^{+}Cl^{-}$ is required to inhibit the respective proteins. In addition, MD simulation studies and MM/GBSA calculations also attribute a prediction for the better inhibition activity of $DAPH^{+}Cl^{-}$ against non-structural nsp2 and nsp-7-nsp8 proteins relative to M^{pro}, although the considerable binding effect was observed for each of the proteins.

At present, structural chromophore-based drug design of different synthetic and commercially available compounds grabs a considerable attraction to scientists. Looking at the severe effect of the SARS-CoV-2, many scientists are actively engrossed in searching for potential therapeutics against SARS-CoV-2 (Culletta et al., 2020, Choudhary et al., 2020, Badavath et al., 2020 and references there in)[60–62]. Culletta et al.[60], explored the inhibition properties of a large number of designed structure-based pharmacophores against the proteins encoded by SARS-CoV-2. They considered 26 experimental drugs, 5 investigational drugs, and 3 approved drugs to study. They carried out molecular docking and MM-GBSA calculations using MD simulations for 100 ns. The drug molecules showed a significant change of dG Bind energy ranging from − 35 to − 90 kcal/mol with the interaction of M^{pro} and nsp proteins. Om Silakari et al.[61], examined the inhibitory properties of a large number of arbidol analogues (36 molecules) through virtual screening of the proteins of SARS-CoV-2 and reported dG bind energies for the docked complexes through MM-GBSA calculations. Among the studied molecules, A_BR4, A_BR9, A_BR18, A_BR22 were highly interactive with spike proteins and A_BR5, A_BR6, A_BR9, and A_BR18 were effective against the main protease of the SARS-CoV-2. The group further reported the ΔG MM-GBSA energies (kcal/mol) for the main protease docked complexes ranging from − 2 to − 47 kcal/mol. Similarly, Badavath et al.[62], forecasts a computer-aided drug design for the anti-SARS screening activity of 118 isatin derivatives comprising 16 distinct heterocyclic compounds, 5 natural products and 7 repurposed drugs. The binding propensities of the compounds towards the main protease of SARS-CoV-2 reveal their potential inhibition properties against SARS-CoV-2. Furthermore, Purwati et al.[63], evaluated the in vitro anti-SARS-COV-2 activity of a series of ratiometrically designed dual combinatory drugs namely Lopinavir–Ritonavir–Clarithromycin, Lopinavir–Ritonavir–Azithromycin, Lopinavir–Ritonavir–Doxycycline, Hydroxychloroquine–Azithromycin, Flaviptravir–Azithromycin against Vero cell lines. The group also determined the cytotoxic concentrations (CC_{50}) and IC_{50} values for 24, 48 and 72 h. They reported the CC_{50}values in the range 4.2×10^{2} to 1.1×10^{10} µg/mL and IC_{50} values ranging from 12.1 to 24.90 µM. The in vitro cytotoxicity studies of $DAPH^{+}Cl^{-}$ against VeroE6 cell lines showed a non-cytotoxic concentration, 12 µM which enabled 70% inhibition against VeroE6 cell lines.

Nevertheless, on comparison of the binding propensities of the molecules with main protease and non-structural proteins of SARS-CoV-2, it is evident that the synthetic hydrated $DAPH^{+}Cl^{-}$ compound shows a good binding effect with main protease (− 19.2 ± 0.3 kcal/mol), nsp2 (− 25.7 ± 0.1 kcal/mol) and nsp7-nsp8 (− 24.5 ± 0.7 kcal/mol) as revealed from MM-GBSA calculations. The changes of binding energies of $DAPH^{+}Cl^{-}$ with M^{pro}, nsp2 and nsp7-nsp8 proteins are considerable with respect to the reported binding energy values of the reported drugs and clinically approved agents. Furthermore, in silico and in vitro cell viability and immunofluorescence assay of $DAPH^{+}Cl^{-}$ against Vero cell lines attributes a good estimation for $DAPH^{+}Cl^{-}$ to turn out a potential therapeutic agent against SARS-CoV-2.

Conclusions

To summarize, we synthesized a hydrated phenazinium chloride through straightforward catalytic oxidation of o-phenylenediamine. Interestingly, we are able to isolate the compound in single crystalline phase in high yield. The crystal structure analysis of the compound reveals that phenazinium ion is stabilized by a chloride ion in association with lattice water. The hydrated $DAPH^{+}Cl^{-}$ compound turns out to be a good bactericidal agent against few clinical bacteria. The synthetic compound displays a comparable MIC value with respect to a standard antibiotic, tetracycline, and can destroy the bacterial cell membrane. Further, in vitro SARS-CoV-2 screening activities were evaluated against 1 × 10e4VeroE6 cells through cell viability assay and cytotoxic studies. The synthetic phenazinium salt exhibits ~ 90% cell viability and 70% inhibition activity at the non-cytotoxic concentration, 12 µM, which is comparable to the SARS-CoV-2 screening activity of remdesivir at 10 µM. The molecular docking studies predict a relatively higher binding propensity of $DAPH^{+}Cl^{-}$ non-structural proteins (nsp2 and nsp7-nsp8) compared to M^{pro}. Different non-covalent interactions like hydrogen bonding, vdw interactions and π-sigma interactions are operative to form stable docked complexes. The MD simulation studies in triplicate for 100 ns show a considerable binding energies (dG Bind) of $DAPH^{+}Cl^{-}$ with nsp2, nsp7-nsp8 and M^{pro} as − 25.7 ± 0.1, − 24.5 ± 0.7 and − 19.2 ± 0.3 kcal/mol, respectively. The binding energies estimated by molecular docking and MD simulations analysis set a similar trend of stability for docked complexes and attribute the stable conformations of $DAPH^{+}Cl^{-}$ docked main protease and non-structural proteins complexes. Finally, we deeply believe that in silico SARS-COV-2 screening activity and in vitro cytotoxicity against VeroE6 cell lines put a new source of light for suitable structural modifications like extension of aromatization or planarity of the phenazine pharmacophore that may certainly enrich the antiviral activity and may turn out to be a potential therapeutics with a great promise.

Data availability

The data are available from the corresponding author upon reasonable request.

Received: 26 June 2021; Accepted: 8 November 2021
Published online: 30 November 2021

References

1. Behera, B. C., Mishra, R. R. & Thatoi, H. Recent biotechnological tools for diagnosis of corona virus disease: A review. *Biotechnol. Prog.* **37**, e3078 (2021).
2. Arabi, Y. M., Balkhy, H. H. & Hayden, F. G. Middle east respiratory syndrome. *N. Engl. J. Med.* **376**, 584–594 (2017).
3. Skariyachan, S., Challapilli, S. B., Packirisamy, S., Kumargowda, S. T. & Sridhar, V. S. Recent aspects on the pathogenesis mechanism, animal models and novel therapeutic interventions for middle east respiratory syndrome coronavirus infections. *Front. Microbiol.* **10**, 569 (2019).
4. International Committee on Taxonomy of Viruses (ICTV). *Naming the 2019 Coronavirus 2020*. https://talk.ictvonline.org/]
5. Kahn, J. S. & McIntosh, K. History and recent advances in coronavirus discovery. *Pediatr. Infect. Dis. J.* **24**, S223–S227 (2005).
6. Monto, A. S. Medical reviews. Coronaviruses. *Yale J. Biol. Med.* **47**, 234–251 (1974).
7. Coelho, C., Gallo, G., Campos, C. B. & Hardy, L. & Würtele, M 2020 Biochemical screening forSARS-CoV-2 main protease inhibitors. *PLOS ONE* **15**, e024007 (2020).
8. Yuan, Y., *et al.* COVID-19-related stigma and its sociodemographic correlates: a comparative study. *Glob. Health,* **17**, 54 (2021).
9. Pedersen, S. F. & Ho, Y. C. SARS-CoV-2: A storm is raging. *J. Clin. Invest.* **130**, 2202–2205 (2020).
10. Huang, C. *et al.* Clinical features of patients infected with 2019 novel coronavirus in Wuhan, China. *Lancet* **395**, 497–506 (2020).
11. Li, R. *et al.* Substantial undocumented infection facilitates the rapid dissemination of novel coronavirus (SARS-CoV2). *Science* **368**, 489–493 (2020).
12. Peiris, J. S., Yuen, K. Y., Osterhaus, A. D. & Stöhr, K. The severe acute respiratory syndrome. *N Engl J Med.* **349**, 2431–2441 (2003).
13. World Health Organization. *WHO Director-General's Opening Remarks at the Media Briefing on COVID-19–11 March 2020* (2020d). https://www.who.int/dg/speeches/detail/who-director-general-s-opening-remarks-at-the-mediabriefing-on-covid-19%2D%2D-11-march-2020. Accessed 11 Mar 2020.
14. Pedersen, S. F. & Ho, Y. C.SARS-CoV-2: A storm is raging. *J. Clin. Invest.* **130**, 2202–2205 (2020).
15. Yan, R., Zhang, Y., Li, Y., Xia, L. & Guo, Y. Q. Zhou, Structural basis for the recognition of SARS-CoV-2 by full-length human ACE2. *Science* **367**, 1444–1448 (2020).
16. Hadjadj, J. *et al.* Impaired type I interferon activity and inflammatory responses in severe COVID-19 patients. *Science* **369**, 718–724 (2020).
17. Olagnier, D. SARS-CoV2-mediated suppression of NRF2-signaling reveals potent antiviral and anti-inflammatory activity of 4-octyl-itaconate and dimethyl fumarate. *Nat. Commun.* **11**, 4938 (2020).
18. Channappanavar, R. & Perlman, S. Pathogenic human coronavirus infections: Causes and consequences of cytokine storm and immunopathology. *SeminImmunopathol* **39**, 529–539 (2017).
19. Wang, F. *et al.* The laboratory tests and host immunity of COVID-19 patients with different severity of illness. *JCI Insight*, **5** ,e137799 (2020).
20. Galani, I. E. *et al.* Untuned antiviral immunity in COVID-19 revealed by temporal type I/III interferon patterns and flu comparison. *Nat. Immunol.* **22**, 32–40 (2021).
21. Saichi, M. *et al.* Single-cell RNA sequencing of blood antigen-presenting cells in severe COVID-19 reveals multi-process defects in antiviral immunity. *Nat. Cell Biol.* **23**, 538–551 (2021).
22. Su, H. *et al.* Identification of pyrogallol as a warhead in design of covalent inhibitors for the SARS-CoV-2 3CL Protease. *Nat. Commun.* **12**, 3623 (2021).
23. Yoshino, R., Yasuo, N. & Sekijima, M. Identification of key interactions between SARS-CoV-2 main protease and inhibitor drug Candidates. *Sci. Rep.* **10**, 12493 (2020).
24. Ahmadi, A. & Moradi, S. In silico analysis suggests the RNAi-enhancing antibiotic enoxacin as a potential inhibitor of SARS-CoV-2 infection. *Sci. Rep.* **11**, 10271 (2021).
25. Paul, P. *et al.* Circumstantial overdose management of an efficient cancer cell photosensitizer with preclinical evidence: A biophysical study. *ACS Appl. Bio Mater.* **3**, 8049–8060 (2020).
26. Laursen, J. B. & Nielsen, J. Phenazine natural products: Biosynthesis, synthetic analogues, and biological activity. *Chem. Rev.* **104**, 1663–1685 (2004).
27. Vilaplana, L. & Marco, M. P. Phenazines as potential biomarkers of pseudomonas aeruginosa infections: Synthesis regulation, pathogenesis and analytical methods for their detection. *Anal. Bioanal. Chem.* **412**, 5897–5912 (2020).
28. Borrero, N. V. *et al.* Phenazine antibiotic inspired discovery of potent bromophenazine antibacterial agents against *Staphylococcus aureus and Staphylococcus epidermidis*. *Org. Biomol. Chem.* **12**, 881 (2014).
29. Rewcastle, G. W., Denny, W. A. & Baguley, B. C. Potential antitumor agents. 51. Synthesis and antitumor activity of substituted phenazine-1-carboxamides. *J. Med. Chem.* **30**, 843–851 (1987).
30. Guttenberger, N., Blankenfeldt, W. & Breinbauer, R. Recent developments in the isolation, biological function, biosynthesis, and synthesis of phenazine natural products. *Appl. Microbiol. Biotechnol.* **25**, 6149–6166 (2017).
31. Pierson, L. S. III. & Pierson, E. A. Metabolism and function of phenazines in bacteria: Impacts on the behavior of bacteria in the environment and biotechnological processes. *Appl. Microbiol. Biotechnol.* **86**, 1659–1670 (2010).
32. Schiessl, K. T. *et al.* Phenazine production promotes antibiotic tolerance and metabolic heterogeneity in *Pseudomonas aeruginosa* biofilms. *Nat. Commun.* **10**, 762 (2019).
33. Biessy, A. & Filion, M. Phenazines in plant-beneficial *Pseudomonas* spp.: Biosynthesis, regulation, function and genomics. *Environ. Microbiol.* **20**, 3905–3917 (2018).
34. Biswas, B., *et al.* Efficient and Selective oxidation of primary and secondary alcohols using an iron(III)/phenanthroline complex: Structural studies and catalytic activity. *Eur. J. Inorg. Chem.* 4479–4485 (2012).
35. CrysAlisPro 1.171.39.35c. *Rigaku Oxford Diffraction* (Rigaku Corporation, Tokyo, Japan, 2017).
36. Sheldrick, G. M. SHELXT-Integrated space-group and crystal-structure determination. *Acta Cryst.* **A71**, 3 (2015).
37. Sheldrick, G. M. Crystal structurerefinement with SHELXL. *Acta Cryst.* **C71**, 3 (2015).
38. Dolomanov, O. V., Bourhis, L. J., Gildea, R. J., Howard, J. A. K. & Puschmann, H. *OLEX2*: A complete structure solution, refinement and analysis program. *J. Appl. Cryst.* **42**, 339 (2009).
39. Turner, M. J., McKinnon, J. J., Wolff, S. K., Grimwood, D. J., Spackman, P. R., Jayatilaka, D.&Spackman, M. A. *Crystal Explorer* (University of Western Australia, 2017). http://hirshfeldsurface.net17.
40. Spackman, M. A. & Jayatilaka, D. Hirshfeld surface analysis. *Cryst. Eng. Com.* **11**, 19–32 (2009).
41. Varnaitė, R. *et al.* Expansion of SARS-CoV-2–specific antibody-secreting cells and generation of neutralizing antibodies in hospitalized COVID-19 patients. *J. Immunol.* **205**, 2437–2446 (2020).

42. Lipinski, C. A., Lombardo, F., Dominy, B. W. & Feeney, P. J. Experimental and computational approaches to estimate solubility and permeability in drug discovery and development settings. *Adv. Drug Deliv. Rev.* **46**, 3–26 (2001).
43. Swiss ADME. http://www.swissadme.ch. Accessed 10 July2020.
44. Ertl, P., Rohde, B. & Selzer, P. Fast calculation of molecular polar surface area as a sum of fragment-based contributions and its application to the prediction of drug transport properties. *J. Med. Chem.* **43**, 3714–3717 (2000).
45. Bowers, K. J., *et al.* [Paper presentation]. *SC'06: Proceedings of the2006 ACM/IEEE Conference on Supercomputing*. 43 (Tampa, FL, USA, 2006; November 1–17).
46. Chow, E., *et al.* DE Shaw Research Technical Report DESRES/TR-2008-01. http://deshawresearch.com. (2008).
47. Shivakumar, D. *et al.* Prediction of absolute solvation free energies using molecular dynamics free energy perturbation and the OPLS force field. *J. Chem. Theory Comput.* **6**, 1509–1519 (2010).
48. Jorgensen, W. L., Maxwell, D. S. & Rives, J. T. Development and testing of the OPLS all-atom force field on conformational energetics and properties of organic liquids. *J. Am. Chem. Soc.* **118**, 11225–11236 (1996).
49. Martyna, G. J., Klein, M. L. & Tuckerman, M. Nosé–Hoover chains: The canonical ensemble via continuous dynamics. *J. Chem. Phys.* **97**, 2635–2643 (1992).
50. Martyna, G. J., Tobias, D. J. & Klein, M. L. Constant pressure molecular dynamics algorithms. *J. Chem. Phys.* **101**, 4177–4189 (1994).
51. Toukmaji, A. Y. & Board, J. A. Jr. Ewald summation techniques in perspective: A survey. *Comput. Phys. Commun.* **95**, 73–92 (1996).
52. Fornera, S. & Walde, P. Spectrophotometric quantification of horseradish peroxidase with *o*-phenylenediamine. *Anal. Biochem.* **407**, 293–295 (2010).
53. Jiang, Y. L. & Feng, C. L. The study on reaction kinetics based on a new system of the horseradish peroxidase catalyting the oxidation of o-phenylenediamine by H_2O_2. *Spectrosc. Spectr. Anal.* **22**, 436–440 (2002).
54. Mahato, S. *et al.* Synthesis, structure, polyphenol oxidase mimicking and bactericidal activity of a zinc-schiff base complex. *Polyhedron* **194**, 114933 (2021).
55. Roy, S. *et al.* Cascade detection of fluoride and bisulphate ions by newly developed hydrazine functionalized Schiff bases. *J. Mol. Liq.* **326**, 115293 (2021).
56. Folgueira, M. D., Luczkowiak, J., Lasala, F., Rivilla, A. P. & Delgado, R. Prolonged SARS-CoV-2 cell culture replication in respiratory samples from patients with severe COVID-19. *Clin. Microbiol. Infect.* **27**, 886–891 (2021).
57. Hosseini, M., Chen, W., Xiao, D. & Wang, C. Computational molecular docking and virtual screening revealed promising SARS-CoV-2 drugs. *Precision Clin. Med.* **4**, 1–16 (2021).
58. Halder, U. C. Predicted antiviral drugs Darunavir, Amprenavir, Rimantadine and Saquinavir can potentially bind to neutralize SARS-CoV-2 conserved proteins. *J. Biol. Res.* https://doi.org/10.1186/s40709-021-00149-2 (2021).
59. Dash, R. *et al.* Structural and dynamic characterizations highlight the deleterious role of SULT1A1 R213H polymorphism in substrate binding. *Int. J. Mol. Sci.* **20**, 6256 (2019).
60. Culletta, G. *et al.* Exploring the SARS-CoV-2 proteome in the search of potential inhibitors via structure-based pharmacophore modeling/docking approach. *Computation* **8**, 77. https://doi.org/10.3390/computation8030077 (2020).
61. Choudhary, S. & Silakari, O. Scaffold morphing of arbidol (umifenovir) in search of multi-targeting therapy halting the interaction of SARS-CoV-2 with ACE2 and other proteases involved in COVID-19. *Virus Res.* **289**, 198146 (2020).
62. Badavath, V. N. *et al.* Determination of potential inhibitors based on isatin derivatives against SARS-CoV-2 main protease (M^{pro}): A molecular docking, molecular dynamics and structure-activity relationship studies. *J. Biomol. Struct. Dyn.* https://doi.org/10.1080/07391102.2020.1845800 (2020).
63. Purwati, *et al.* An in vitro study of dual drug combinations of anti-viral agents, antibiotics, and/or hydroxychloroquine against the SARS-CoV-2 virus isolated from hospitalized patients in Surabaya. *Indonesia. PLOS ONE.* https://doi.org/10.1371/journal.pone.0252302 (2021).

Acknowledgements

Dr. Bhaskar Biswas gratefully acknowledge the financial support received from the University of North Bengal, Darjeeling 734013. The authors sincerely thank to the Advanced Technology Platform Centre, Regional Centre for Biotechnology, Faridabad, India for carrying out the in vitro antiviral studies of the synthetic compound against VeroE6 cell. The authors sincerely acknowledge the Centre for Biotechnology and Phyto Pharmacognosy Research, Coimbatore, India, for supporting the measurement of biological activities. The authors sincerely thank Dr. Om Silakari of Molecular Modelling Lab (MML), Department of Pharmaceutical Sciences and Drug Research, Punjabi University, Punjab-147002, India for the valuable discussion on in silico SARS-CoV-2 screening activity of the synthetic compound.

Author contributions

All authors made substantial contributions to the study and manuscript preparation. B.B. and S.B. developed the concept of the study. All authors approve this version of the manuscript for publication.

Competing interests

The authors declare no competing interests.

Additional information

Supplementary Information The online version contains supplementary material available at https://doi.org/10.1038/s41598-021-02280-5.

Correspondence and requests for materials should be addressed to S.B. or B.B.